Precise Alignment of Micromachined Electrode Arrays With V1 Functional Maps

Ian Nauhaus and Dario L. Ringach

J Neurophysiol 97:3781-3789, 2007. First published Mar 7, 2007; doi:10.1152/jn.00120.2007

J Neurophysiol 97: 3781–3789, 2007.
First published March 7, 2007; doi:10.1152/jn.00120.2007.

Precise Alignment of Micromachined Electrode Arrays With V1 Functional Maps

Ian Nauhaus[1] and Dario L. Ringach[2]

[1]*Departments of Biomedical Engineering and* [2]*Psychology, University of California, Los Angeles, California*

Submitted 2 February 2007; accepted in final form 27 February 2007

Nauhaus I, Ringach DL. Precise alignment of micromachined electrode arrays with V1 functional maps. *J Neurophysiol* 97: 3781–3789, 2007. First published March 7, 2007; doi:10.1152/jn.00120.2007. Recent theoretical models of primary visual cortex predict a relationship between receptive field properties and the location of the neuron within the orientation maps. Testing these predictions requires the development of new methods that allow the recording of single units at various locations across the orientation map. Here we present a novel technique for the precise alignment of functional maps and array recordings. Our strategy consists of first measuring the orientation maps in V1 using intrinsic optical imaging. A micromachined electrode array is subsequently implanted in the same patch of cortex for electrophysiological recordings, including the measurement of orientation tuning curves. The location of the array within the map is obtained by finding the position that maximizes the agreement between the preferred orientations measured electrically and optically. Experimental results of the alignment procedure from two implementations in monkey V1 are presented. The estimated accuracy of the procedure is evaluated using computer simulations. The methodology should prove useful in studying how signals from the local neighborhood of a neuron, thought to provide a dominant feedback signal, shape the receptive field properties in V1.

INTRODUCTION

Primary visual cortex is organized into functionally distinct columns normal to the surface (Hubel and Wiesel 1962). In vivo two photon imaging is now revealing very precise layouts of orientation at very small scales (Ohki et al. 2005, 2006). Tangential to the cortex, the structure of orientation maps are very smooth except for localized, sharp transitions (orientation fractures and singularities) having widths comparable with that of a single cell body. In a direction normal to the cortex, as deep as it can be imaged using today's technology, there is a very precise alignment for preferred orientations along a column (Ohki et al. 2006).

A question that has received increased interest is how feedback from the local neighborhood of a cell may shape its response properties (Marino et al. 2005; Schummers et al. 2002). This is an important issue because it can shed light onto the question of how feedforward and feedback signals shape the tuning of cortical cells (Ferster and Miller 2000; Sompolinsky and Shapley 1997). Recent network models of macaque V1, for example, predict specific relationships between a neuron's location within the orientation map and response properties such as total conductance, firing rate, and orientation tuning selectivity (McLaughlin et al. 2000, 2003). Given that the spatial extent of local connections is <500 μm (Callaway 1998; Lund 1987; Yoshioka et al. 1996), the local neighborhood can be summarized, as a first approximation, by the distribution of preferred orientations in the orientation map within such a window (e.g., Marino et al. 2005).

To study how the local network influences the responses of cortical neurons, previous studies have relied on single electrode penetrations aimed at either orientation singularities (pinwheel centers) or iso-orientation domains. This is normally performed by first superimposing orientation maps with images of the surface vasculature. Salient points of the vasculature are used for visually guiding the electrode penetration to target locations on the map. In principle, this method can incur significant errors derived from the parallax (caused by a discrepancy in viewing angle between the imaging camera and the surgical microscope) and from non-normal penetration angle of the electrodes. This problem is compounded by the curvature of the cortex and the fact that the vasculature may not lie directly on the surface. To our knowledge, no previous study has offered a rigorous analysis of the errors involved in visual targeting of electrodes.

The goal of this study is to offer a novel method that allows the precise alignment of electrophysiological recordings form micromachined arrays with functional maps obtained by intrinsic imaging. The basic idea is simple. After an orientation map is obtained, a micromachined array is implanted in the same patch of cortical tissue. Orientation tuning curves are obtained from all electrodes that yield visually driven responses. Using 10×10 electrode arrays, we normally obtained $\sim$50 electrodes with reliable orientation tuning. The location of the array is parameterized by three numbers, its translation, and rotation (we will also consider more complex models that include tilt and slant). The location of the array is estimated by finding the optimal translation and rotation that maximize the agreement between the preferred orientations measured at the tip of a subset of electrodes and those measured optically. Because the number of data points ($\sim$50) is much higher than the number of unknowns (the 3 parameters for the array location) the problem is vastly overdetermined. As a consequence, the algorithm is found to be very robust to noise in the estimates of preferred orientations. We further show that the optimization has a well-defined solution and is accurate to $\sim$20 μm (the diameter of a single cell body). This new methodology should provide a better experimental handle to study how local feedback signals originating from the local neighborhood of a neuron influence its function.

Address for reprint requests and other correspondence: I. Nauhaus, Dept. of Neurobiology, 73-210 CHS, University of California, Los Angeles, CA 90095-1763.

The costs of publication of this article were defrayed in part by the payment of page charges. The article must therefore be hereby marked "*advertisement*" in accordance with 18 U.S.C. Section 1734 solely to indicate this fact.

METHODS

Animal preparation

All experiments were approved by UCLA Animal Research Committee and were carried out following National Institutes of Health's Guidelines for the Care and Use of Mammals in Neuroscience. Acute experiments were performed on anesthetized and paralyzed adult Old World monkeys (*Macaca fascicularis*). Initially, the animal was sedated with acepromazine (30–60 μg/kg), anesthetized with ketamine (5–20 mg/kg, im) in the cage, and transported to the surgical suite. Initial surgery and preparation were performed under isofluorane (1.5–2.5%). Two intravenous lines were put in place for the infusion of fluids and drugs. A urethral catheter was inserted to collect and monitor urine output, and an endotracheal tube was inserted to allow for artificial respiration. All surgical cut-down sites were infused with local anesthetic (xylocane, 2%, sc). Pupils were dilated with ophthalmic atropine, and custom-made gas permeable contact lenses were fitted to protect the corneas. After this initial surgery, the animal was transferred to a stereotaxic frame. At this point, anesthesia was switched to a combination of sufentanil (0.05–0.2 μg/kg/h) and propofol (2–6 mg/kg/h). We proceeded to perform a craniotomy over primary visual cortex. The animal was paralyzed (pavulon, 0.1 mg/kg/h) only after all surgical procedures were complete. To ensure a proper level of anesthesia throughout the duration of the experiment, rectal temperature, heart rate, noninvasive blood pressure, end-tidal CO_2, and EEG were continually monitored through an HP Virida 24C neonatal monitor. Urine output and specific gravity were measured every 4–5 h to ensure adequate hydration. Drugs were administered in balanced physiological solution at a rate to maintain a fluid volume of 5–10 ml/kg/h. Rectal temperature was maintained by a self-regulating heating pad at 37.5°C. Expired CO_2 was maintained between 4.5 and 5.5% by adjusting the stroke volume and ventilation rate. The maximal pressure developed during the respiration cycle was monitored to ensure that there was no incremental blocking of the airway. A broad-spectrum antibiotic (bicillin, 50,000 IU/kg) and anti-inflammatory steroid (dexamethasone, 0.5 mg/kg) were given at the beginning of the experiment and every other day.

Optics and visual stimulation

Stimuli were generated on a Silicon Graphics O2 and displayed on a monitor at a refresh rate of 100 Hz and a typical screen distance of 80 cm. The mean luminance was 60 cd/m^2. A Photo Research Model 703-PC spectro-radiometer was used for calibration. The eyes were initially refracted by direct ophthalmoscopy to bring the retinal image into focus for a stimulus roughly 80 cm from the eyes. Optical imaging of intrinsic signals was performed using this refraction. After the array was implanted, and neural responses were isolated, we measured spatial frequency tuning curves and maximized the response at high spatial frequencies by changing external lenses in steps of 0.25 D. This procedure was performed independently for both eyes. The optimal refraction used for all subsequent electrophysiological measurements was always within 0.5 D of the initial estimate obtained by direct ophthalmology.

Optical imaging

Our imaging setup consists of a Dalsa 1M60 camera (Dalsa, Ontario, Canada) fitted with a 55-mm telecentric lens (Edmund Optics). The use of a telecentric lens that minimizes perspective distortion is important, because any distortion of the map would adversely affect any alignment procedure. Spatial distortion in our setup was <1%. Depth of field in our setup was ~0.5 mm, and the camera was positioned through a computer-controlled motorized linear stage (Edmund Optics) to optimally focus on the small blood vessels at the surface of the cortex. For image acquisition, we used a Matrox Helios Camera-Link frame grabber (Matrox, Quebec, Canada) and the Matrox Imaging Library to create a custom interface within Matlab (Mathworks) to run our experiments. For illumination, we used Illumination Technologies (East Syracuse, NY) 3900 Smart-Lite illuminator with appropriate focusing lenses to achieve an even illumination across the cortical surface. Vasculature images were obtained using a green filter, whereas intrinsic images were obtained using red illumination and a 700-nm filter with 20-nm bandwidth (58460, Spectra Physics, Mountain View, CA).

Orientation maps were obtained using the classical presentation scheme described in Bonhoeffer and Grinvald (1991). Drifting gratings are presented at eight equally spaced orientations in both directions (16 conditions). Each condition is presented ~30 times for 3 s, followed by a 5-s "blank" to bring the hemodynamic signal back to baseline. We observe the trial-averaged response of individual pixels on-line. The 5-s rest period is generally sufficient but is adjusted during the experiment accordingly. The average response to each condition is computed within a time window after the stimulus onset of ~2–4 s. The average responses to each condition are added together as a vector sum. For each pixel, this summation is shown as $\Sigma_c\, r(c)e^{i2\theta(c)}$, where $r(c)$ is the average response to a condition, and $\theta(c)$ is the angle of orientation for a given condition. The angle of the preferred orientation is the resultant, divided by 2. The vector image is processed with a spatial band-pass filter constructed as the difference of a two-dimensional (2-D) Gaussian (σ = 75 μm) and a uniform disc (diameter = 1,500 μm). This processing is conservative given that the periodicity of the maps is typically on the order of ~800 μm. Figure 1*A* shows a typical response to gratings at 0°, minus the mean response to 90°, divided by the mean response to all gratings (i.e., the "cocktail blank"). The relative magnitude change in reflectance of 0.25% is comparable with what has been reported in previous studies.

The optical chamber must be removed after the imaging to make room for the cables of the electrode array. This eliminates the possibility of using permanent adhesives, such as dental cement. We found a simple solution where a ring of sterile bone wax was molded into a chamber around the craniotomy. A circular glass coverslip was pressured against the top to seal the chamber. The chamber was filled with 1% agarose by impaling the wax with a syringe after having made another small opening to allow air to exit.

Array recordings

Once the optical imaging experiment was complete, the chamber was removed to prepare for the Cyberkinetics 10 × 10 electrode array (400-μm separation and 1.5-mm electrode length). The array connectors were first mechanically stabilized so the array tips were just touching the top of the cortical surface. The surface tension that develops between saline and the array was normally sufficient to hold the array in place. Of course, it was not possible to aim the array at a particular location within the orientation map. One simply has to ensure that the array is inserted within the boundaries of the imaged portion of the cortex. To avoid excessive cortical damage, the arrays were inserted at high speeds (~8 m/s) using a specially designed pneumatic insertion device (Rousche and Normann 1992). The settings on the insertion device were such that the array was only partially inserted. Visual estimates of the insertion depth were ~1 mm. A typical insertion sequence is shown in Fig. 1*B*, including *1*) the durotomy, *2*) the positioning of the array, *3*) the pneumatic insertion, and *4*) the inserted array.

The array and surrounding tissue were covered in 1.5% agar to improve stability. After the array was inserted, the camera used during optical imaging was brought back to the same approximate place that the images were taken from and used to obtain a picture of the array inserted in the cortex. This serves the purpose of providing a rough guide to the location of the array that will aid to limit and constrain the search for the optimal location. Single-unit recordings with these arrays can last ~8 h or more. For all experimental data shown, the center of the array was aimed at 6 mm posterior to the lunate sulcus

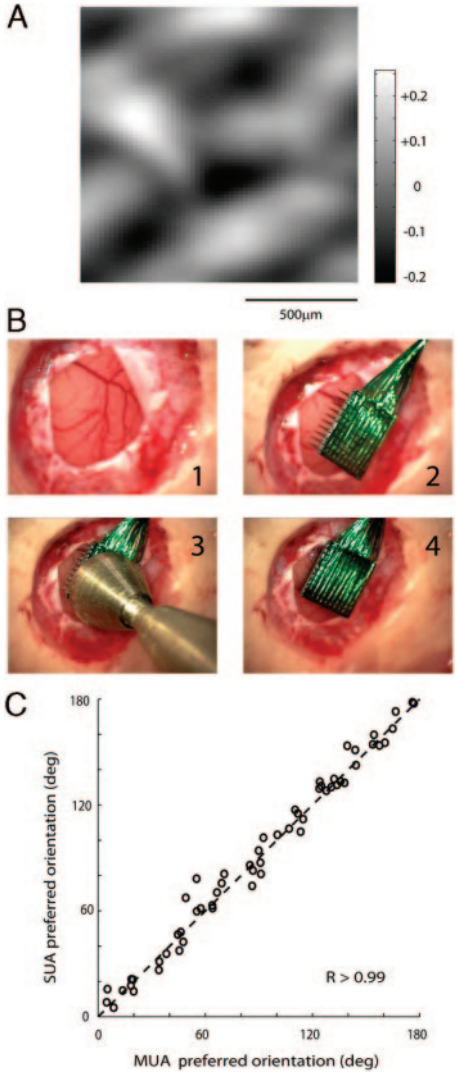

FIG. 1. *A*: typical magnitude of optical imaging in our recordings. Gray-scale image shows average response to 0° oriented gratings minus response to 90° gratings, divided by mean response to all orientations in the experiment. Values are scaled by 100 to represent percent difference in the signal. Similar to other studies, we observed average signals in the order of 0.25%. *B*: typical insertion sequence after imaging: (*1*) durotomy, (*2*) array positioning, (*3*) pneumatic insertion, and (*4*) inserted array. *C*: correlation between preferred orientations of multiunit activity (MUA) and single-unit activity (SUA). Scatter-plot shows correlation between preferred orientations estimated using MUA vs. SUA in electrodes where single cells units were clearly isolated. There is a very high correlation between these estimates, justifying use of MUA in the alignment algorithm.

and 8 mm lateral to the midline. Electrical signals were amplified and spikes discriminated using a Cerebus 128-channel system (Cyberkinetics). Signals that crossed a specified threshold in each electrode were saved to disk for spike-sorting at a later stage. These threshold crossing events are defined as multiunit activity (MUA). Spike sorting was performed through clustering of the first three principal component coefficients. Single-unit activity (SUA) refers to spikes sorted in this way. Orientation tuned responses from MUA were normally present in 50–70 of the electrodes, with single-unit spikes present in about one third to one fourth of these electrodes. A recent report by Kelly et al. (2007) describes the use of these arrays in cortical recordings.

The accuracy of the alignment procedure described below is largely dependent on the number of electrode sites with measurable orientation preference. MUA was used because it invariably allows for a greater number of significantly tuned sites than SUA. By comparing the preferred orientation using MUA with preferred orientation using SUA in those cases where it can be isolated, we established that there is a very high correlation between the two (Fig. 1*C*), justifying the use of MUA for alignment purposes. In our recordings, we typically found >50 electrodes with MUA tuned for orientation.

Visual stimulus and tuning curves

We use a visual stimulus that has proven to be very effective at obtaining orientation tuning curves quickly and accurately. The stimulus consists of rapidly flashed sinusoidal gratings of random orientation, spatial frequency, and spatial phase (Ringach et al. 1997, 2003), presented over all receptive fields simultaneously. This provides the probability distribution of a cell's response to each stimulus in the ensemble, at given time delays [i.e., $K(\theta,\Phi,\Omega|t)$, where θ,Φ,Ω,t are orientation, spatial frequency, spatial phase, and time, respectively]. The preferred orientations were obtained at a time-lag whereby the kernel, as a function of spatial frequency and orientation, has the maximum variance. This optimal time is expressed as $t_{opt} = \max_t \text{var}[\Sigma_\Omega K(\theta,\Phi,\Omega|t)]$. In addition, all computations incorporate a convolution of the kernel with a conservative 3 × 3 smoothing function in the spatial frequency and orientation domain (i.e., after summing over spatial phase). All orientation tuning curves are generated at t_{opt} by summing over the spatial frequency and phase: $R(\theta,t_{opt}) = \Sigma_\Phi\Sigma_\Omega K(\theta,\Phi,\Omega|t_{opt})$. The preferred orientation was obtained from this curve.

Alignment algorithm

Despite the arbitrary placement of the array on the optically imaged cortical surface, there is sufficient information to precisely identify the electrode locations within the orientation map. Given an insertion normal to the cortical surface, the array has three degrees of freedom (x-translation, y-translation, and k-rotation). In RESULTS, we further discuss the ability to account for "slant/tilt" (slant = angle of deviation from a normal insertion; tilt = axis of the slant) by using two additional degrees of freedom. Briefly, the results show that there is minimal slant for our insertions so that x,y,k are an excellent first approximation. Each x,y,k combination provides a unique set of electrode locations and orientation map values. The optimal location (x_o,y_o,k_o), can be defined as the one producing the "best match" between the optically recorded preferred orientations and the electrically recorded preferred orientations from multiunit spikes. The algorithm seeks to minimize the mean-squared error of the orientation differences by varying the array location parameters. Because we have data from many electrodes (normally >50) and only three unknown parameters (x,y,k), the system is vastly overdetermined. This error minimization problem is put into equation form as $\min_{x,y,k}\|e(x,y,k)\|^2 = \min_{x,y,k}\Sigma_{ij}[\theta_{ij} - \Phi_{ij}(x,y,k)]$.[2] The variables x, y, and k are the translation and rotation of the array, θij is the orientation selectivity at electrode position (i,j), and $\Phi_{ij}(x,y,k)$ is the orientation in the pixel image at electrode position (i,j) given the array position (x,y,k). The subtraction is a modular difference that wraps at 90°, because orientation is a cyclic quantity ranging from 0 to 180°. Because this procedure only needs to be done once for each array placement, and because it should be as robust as possible, we used an exhaustive search that computes the error for every x,y,k combination within a liberal range. This ensures that we have located the global minimum and optimal electrode positioning. The range of the search for each degree of freedom is identified with an initial estimate of x_o,y_o,k_o using a picture of the implanted array on the cortical surface. The step size of the search along the x- and y-dimensions is one pixel (25 μm/pixel for all experiments and simulations shown here) and ~0.7° for the k dimension. Simulations show that because the problem is overdetermined, it

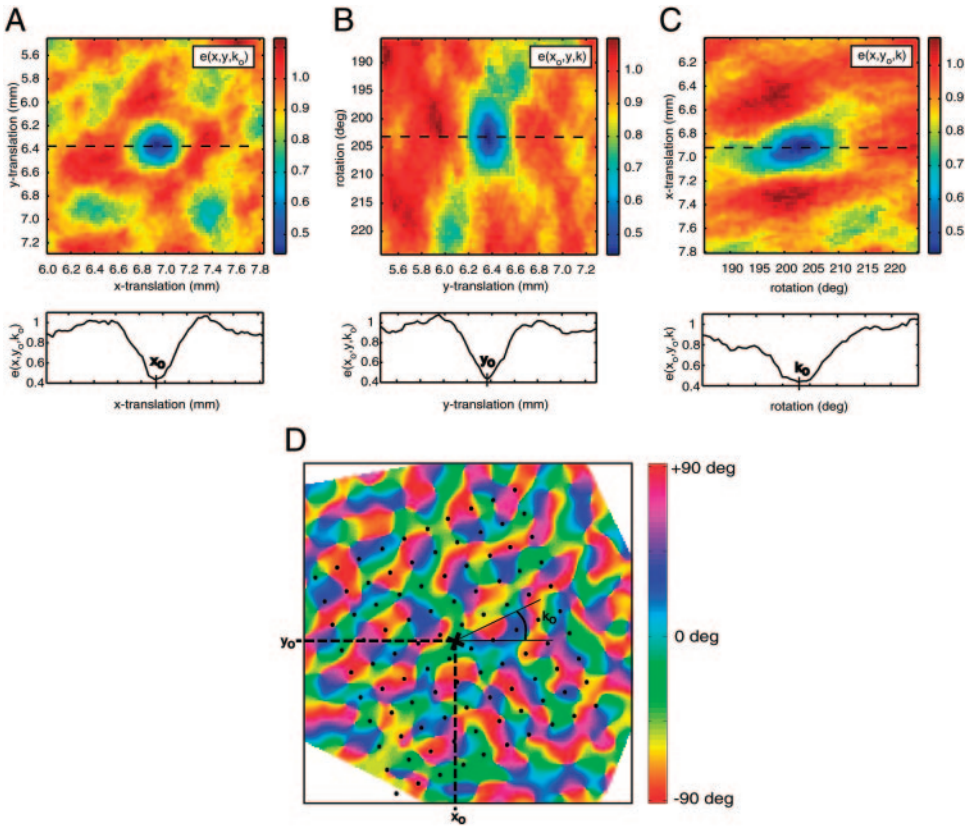

FIG. 2. Experimental results of the proposed alignment method. Before performing the search, an estimate of the array's location is obtained from a picture of the array on the cortical surface that has been registered (using reference points from surrounding tissue) to have a similar perspective as images taken during optical imaging. The search is performed over a liberal range around this initial estimate: ~1.8 mm for both *x*- and *y*-translation and a rotational range of ~40°. Step size is 1 pixel (25 μm) for *x*-translation and *y*-translation and 0.7° for rotation. *A*: image is a 2-dimensional slice through the RMS error function [i.e., $e(x,y,k_o)$]. Dashed line in image crosses minimum error at optimal *y*-translation and represents 1-dimensional function shown below, $e(x,y_o,k_o)$, which displays the location of optimal *x*-translation, x_o. Images in *B* and *C* are also slices taken through location of minimum error but at optimal *x*-translation and *y*-translation. Dip is at an obvious global minimum for all 3° of freedom, which corresponds to location of array shown in *D*. Grid of black dots is electrode positions as determined by x_o,y_o,k_o.

can tolerate large amounts of noise in the measurements and still come up with an accurate estimate of the array's location.

RESULTS

Results of this method from one array insertion are shown in Fig. 2. The image in Fig. 2*A* shows a slice of the root-mean-squared (RMS) difference in orientation preference (radians) between the electrophysiological and optical estimates, as a function of *x*- and *y*-translation at the optimal rotation, $e(x,y,k_o)$. A 1-D slice at the optimal value for *y*-translation, indicated by the dashed line, is shown at the bottom of the panel. The images in Fig. 2, *B* and *C,* are slices of the error surface at the optimal *x*-translation and *y*-translation, respectively. The location of the pronounced dip in these error plots corresponds to the best estimate of the array's location. These values for x_o,y_o,k_o are translated into the positions of the electrodes, as shown in Fig. 2*D*. It can be seen that the electrodes sample from a wide variety of locations within the orientation map, with some being close to orientation singularities, some close to fractures, and some lying within linear zones. Thus the method allows for the comparison between the RF properties of neurons with the local structure of the orientation map.

The sharpness of the dip in the error surface and the absence of obvious local minima are indicative of our ability to accurately determine x_o, y_o, and k_o. A very broad dip would indicate displacement errors on the order of the bandwidth, and multiple local minima (or dips) would suggest relatively large displacement errors caused by the ambiguity of the correct minimum. We note that it would be difficult to quantify such indeterminacy of x_o,y_o,k_o from this data alone, because the RMS error used in these plots may not be linearly related to the uncertainty of array positioning. Other error metrics that are monotonically related to RMS [e.g., log(RMS)] would find the exact same array location but yield different bandwidths for the dip. The likelihood of x_o,y_o,k_o to deviate from the actual location (which can be translated into the expected deviation of the individual electrodes) has been thoroughly quantified with simulations.

The result of applying the method in two different animals is shown in Fig. 3, *A* and *B* (*A* corresponds to the same example shown in Fig. 2). The scatter-plots show the preferred orientation estimated from the optical recordings (*x*-axis) versus the preferred orientation estimated from the multiunit responses (*y*-axis) at the optimal array location. From these data, one can compute the empirical distribution of the orientation errors (Fig. 3*C*), which is well fit by Gaussian with an SD of 18.9°. The variance of this distribution could have multiple causes, including errors of the imaging procedure or errors in estimating the preferred orientation from spike response. Regardless of the cause, a computer simulation shows that the method is extremely robust against noise of this magnitude.

Searching additional degrees of freedom: "slant/tilt"

The degrees of freedom are limited to translation and rotation (x,y,k) under the assumption that the electrodes have been inserted normal to the cortical surface and that the cortex is approximately flat within the spatial extent of the array. A deviation from normal effectively creates a compression of the recording plane along a particular direction. The magnitude of this compression (i.e., slant), and the direction along which it occurs (i.e., tilt), introduces two additional degrees of freedom

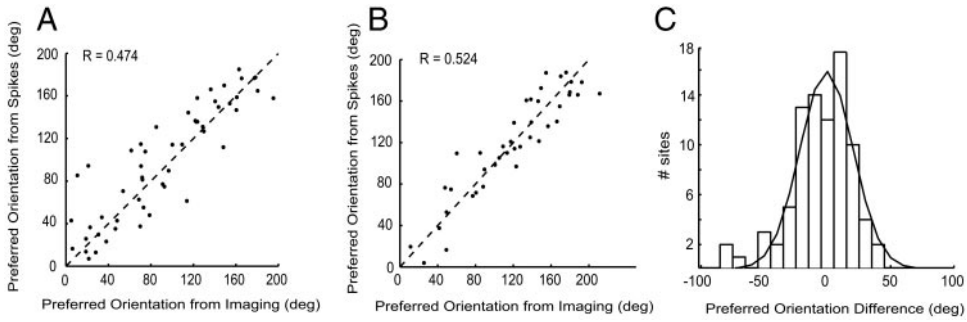

FIG. 3. Orientation scatter from 2 experiments. *A* and *B*: orientation preference from electrophysiology vs. preference in maps at electrode locations determined in the search. Orientation domain is from 0 to 180°. Axes go beyond 180° because circular variables have been "unwrapped" to better show correlation. We used a correlation coefficient metric for angular variables provided by Mardia (1972), which results in *R* values of 0.474 and 0.524 for the 2 experiments. It should be noted that using this correlation metric, instead of error, results in the exact same location of array in the search (i.e., maximizing correlation is equivalent to minimizing error). *C* combines the 2 experiments to create a distribution of difference in orientation. A Gaussian was fitted (red) to the distribution to model inherent noise (SD = 18.9°).

to the array positioning. The effect of slant on the recording plane is shown by the 2-D representation in Fig. 4. Because the "effective width" is proportional to cos(slant°), it is only for relatively large values of slant that the dimensionality of the recording plane becomes significantly effected. For example, a slant of 15° results in a compression of the recording plane of ~100 μm, whereas a slant of 5° compresses the plane by ~14 μm. The ratio of electrode length (1.5 mm) to the width of the array (3.6 mm) allows for a maximum slant of ~22.6° and a compression of ~276 μm. The electrodes can still be accurately localized by incorporating slant and tilt as two additional degrees of freedom in the search algorithm. We checked for such a deviation by performing the search across all five degrees of freedom. For the experiment shown in Fig. 2, this resulted in the same values for *x,y,k* and a slant of ~6°. This very subtle change in the location of (some) electrodes was not enough to improve the correlation shown in Fig. 3*A* by a significant amount. It should be noted that error in electrode localization caused by tilt is also possible in the single-electrode penetration studies using the cortical vasculature. This method allows one to correct for such error when necessary.

Expected accuracy of the technique

How well is the method expected to perform? To answer this question, we did bootstrap simulations to generate statistics on the expected deviation of the measured from actual electrode locations. Because the alignment method relies on correspondence between the electrode recordings and optical imaging, the simulations model the corruption of this correspondence (by measurement error) as the inhibiting factor in the localization. It is not possible to determine the exact source, or statistics, of the noise, so we have implemented two different simulations to help validate the accuracy of the technique: one where the noise is independent across the electrodes and a second one where the noise may depend on the location within the map.

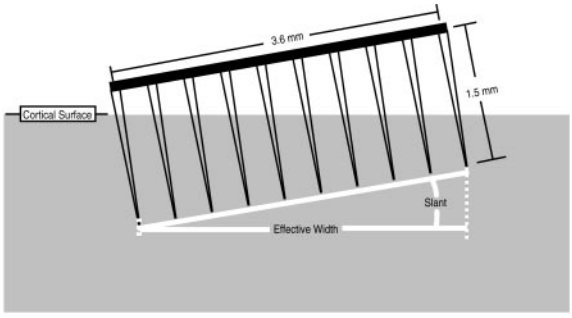

FIG. 4. Effect of slanted implant on recording plane. Effective width is projection of recording plane on cortical surface and is proportional to cosine of slant angle along direction of tilt. Diagram reduces the problem to 2 dimensions and therefore does not show tilt (which corresponds to axis of slant on horizontal plane). If the slant angle is large, the recording plane could be compressed up to ~276 μm, and localization should take this effect into consideration. In our experience, however, good implants result in very small slant angles (in the order of 5°).

The first simulation simply assumes independent noise in the preferred orientation at each electrode by sampling from the experimentally determined distribution in Fig. 3*C*. One can think of this simulation as assuming that the orientation map is noise-free and all the discrepancy between the measured and actual orientations originates from the electrophysiological recordings. It is possible, however, that the noise is dependent on the location within the map: recordings from iso-orientation domains may provide more reliable estimates than recordings near pinwheels or fractures (Hetherington and Swindale 1999). Similarly, mismatches dependent on the orientation map are likely to result from the finite spatial resolution of the optical imaging (Polimeni et al. 2005). This brings us to the second simulation, which takes into account these two factors. The main finding from these simulations is simple: the fact that we have many more data than free parameters (the system is vastly overdetermined), the alignment algorithm is extremely robust to noise.

Simulation 1: additive white Gaussian noise

The first simulation incorporates an estimate of the distribution of noise from the experimental results. That is, once the optimal location of the array from an actual insertion has been determined, the noise is represented as the difference in orientation preference between the imaging and electrophysiology. A Gaussian was fitted to this distribution of orientation error across the electrodes of two experiments (Fig. 3*C*), and the noise is assumed to be additive and independent of the local map structure.

To an artificial dataset, we first arbitrarily decide on the (*x,y,k*) positioning of the array within an experimentally measured orientation map. The assumption is that this orientation

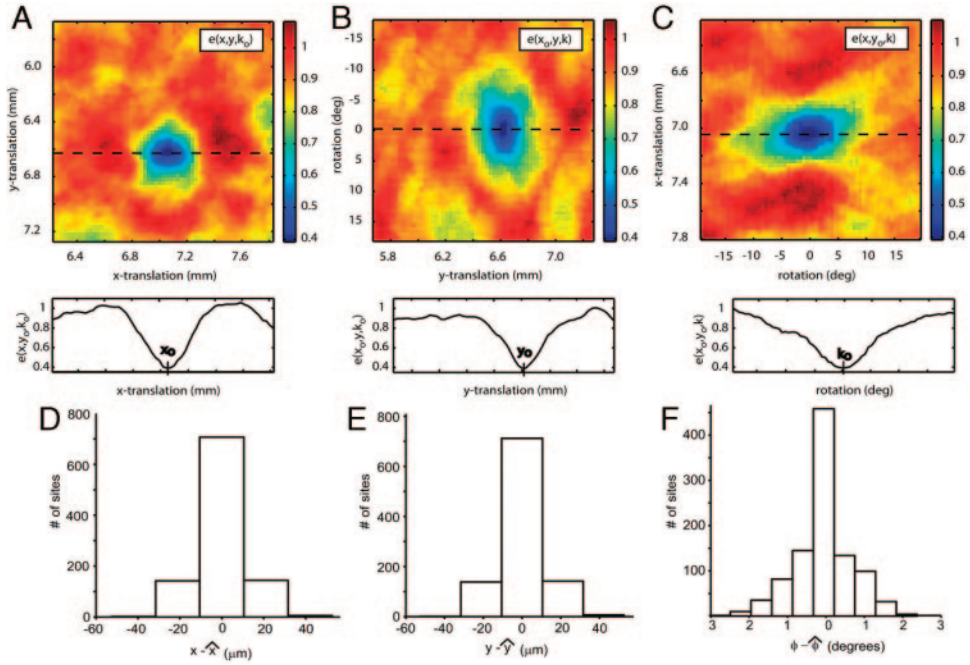

FIG. 5. Electrode alignment simulation using circular white Gaussian noise with an SD of 20° (orientation domain: 0–180°). Noise is added to map values at locations of electrode insertion. Using orientation preference, positioning of the 10 × 10 electrode array is successfully determined by minimizing error. *Top row*: slices in the error block for a single trial. Slices are at optimal rotation (*A*), *x*-translation (*B*), and *y*-translation (*C*). Pronounced dip is at correct location and significantly less than any local minima. *Bottom row*: results of simulation for 1,000 trials showing how peak in error distribution deviates from correct location. *D*: distribution of displacement in array rotation. SD = 0.757°. *E*: distribution of displacement in *x*-translation. SD = 14.75 μm. *F*: distribution of displacement in *y*-translation. SD = 14.70 μm.

map is noise-free. Next, the corresponding 100 electrode locations are computed using the electrode sampling rate (400 μm) and the magnification of the camera (~40 pixels/mm for the images collected in the experiment). These locations are the (*i,j*) variables at the optimal (*x,y,k*), which we will now refer to as (i_o,j_o) and (x_o,y_o,k_o). The camera magnification is precisely verified on all real experiments. (i_o, j_o) allows us to "look up" the corresponding functional values in the map (Φij in the preceding equation). Circular, Gaussian noise, with an SD of 20° (experimental measurement = 18.9°) is added to these functional values to create the simulated dataset for the electrodes. A typical experiment will provide ≤60 electrodes with MUA tuned for orientation. For this simulation, we conservatively chose 50 electrodes at random.

We first provide an example of the error function from a single trial, by displaying slices of the 3-D function, $e(x,y,k)$, in the same fashion as was done in Fig. 2 (Fig. 5, *A–C*). There is a pronounced dip in the error at the optimal position. As in the experimental data, the location of this dip is not absolutely sharp, which implies that the global minimum may be shifted away from the optimal position. We ran this simulation 1,000 times with independent noise to acquire statistics on the influence of such a deviation from the ground truth. Figure 5, *E* and *F,* are distributions of the *x*- and *y*-translation error. In 1,000 trials, the estimated location of the array never shifted by more than two pixels (~50 μm). Figure 5*D* shows the error distribution for rotation. The SD is <1°.

The relationship we are ultimately interested in, however, is how the estimated locations of the individual electrodes deviate from their actual locations. Using the same 1,000 trial simulation above, we were able to determine the corresponding distribution of displacement error for each of the electrodes. On each trial, the displacement vector for the array [i.e., $(x,y,k)_{actual} - (x,y,k)_{estimate}$] can be used to compute the translational shift of all 100 electrodes. That is, a given deviation of *x,y,k* can be mapped to a 2-D deviation for each electrode in the array. This provides 100,000 electrode localization error samples for the 1,000 trials. Because the distribution of determined locations does not have a bias in any particular direction with respect to the actual location, the resultant of these 2-D vectors across all trials has a magnitude of almost zero. The average magnitude of the error vectors, on the other hand, is ~33.16 μm. The distribution of the displacement magnitude is shown in Fig. 6. The error was <58 μm for 90% of the samples and <28 μm for 50% of the samples. It should also be noted that this distribution changes systematically for different locations in the array. That is, the average displacement magnitude is greater for electrodes that are further from the center of the array. The distribution in Fig. 6 pools all electrodes in the array.

Simulation 2: spatial distribution of cells from electrode tip and point spread function from imaging

In this simulation, we assumed that some errors are due to the imaging procedure [e.g., by the point spread function (PSF)

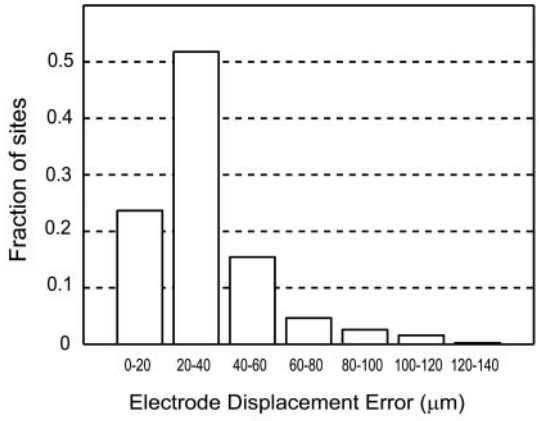

FIG. 6. Distribution of electrode displacement errors. Deviation of estimated location from actual location has a mean of ~33.16 μm. The 90th percentile is at 58 μm, and the 50th percentile is at 28 μm.

of the optics] and the fact that MUA may sample from a number of cells in the local neighborhood. Thus larger discrepancies in orientation preference between the electrophysiology and imaging are more likely to occur near pinwheel centers. To simulate this effect, we used results from experimental and theoretical estimates of voltage decay in the cortex (Gray et al. 1995; Rall 1962). They showed that the drop in voltage with distance from the soma follows an exponential function with a decay constant of ~28 μm. To create the multiunit orientation preference, we computed a vector sum of the pixels in the orientation map around the actual electrode location. The sum was over an area of radius 65 μm. This is the distance at which a cell voltage decays by 90%, given the theoretical decay constant. To create the second source of noise, imaging blur, we convolve a PSF with the vector image used to display the actual orientation preference map. This is mathematically equivalent to a spatial convolution with each of the images taken during the experiment and before computing the resulting vector image. The full-width half-maximum (FWHM) of the PSF has been estimated to be from 50 to 240 μm (Grinvald et al. 1999; Orbach and Cohen 1983; Polimeni et al. 2005). We provide results using a distribution of PSF bandwidths that encompass this range (Fig. 7).

The results for the distribution of the translation and rotation errors were similar to that shown in Fig. 5 of the previous simulation. That is, the displacement errors for the array's three degrees of freedom were rarely >20 μm, or 1° of rotation. Here, we show the theoretical distributions of electrode displacement for four different amounts of spatial blur (bandwidth of a Gaussian PSF). Naturally, the distribution gets pushed to higher values as the FWHM goes up, as shown in Fig. 7. Table 1 summarizes the results. The second column is the mean of each distribution in microns, and the third and fourth columns are the values under which 90 and 50% of the displacements will occur. Even in the worst-case scenario (a FWHM of 240 μm), the simulation suggested that the electrodes will deviate by <56.8 μm 90% of the time. In addition, these results show

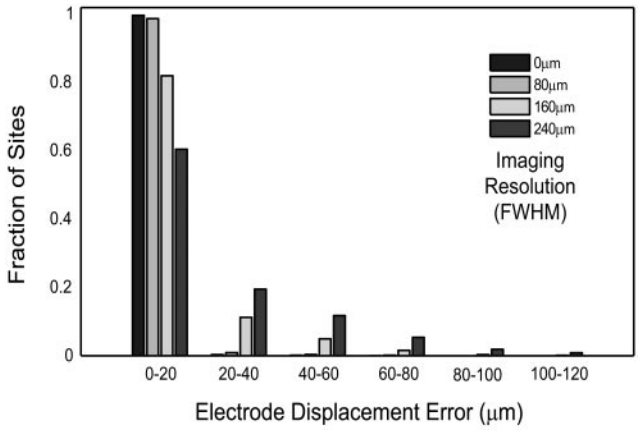

FIG. 7. Distributions of electrode displacement magnitude for 4 different point spread function (PSF) full-width half-maximums (FWHMs). Distributions get skewed to higher values as imaging resolution drops. However, even for an FWHM of 240 μm, average error is only 22.3 μm. This figure also shows that the multiunit sample space has little affect on localization accuracy because displacement error is essentially 0 μm under infinite imaging resolution (FWHM = 0 μm). Statistics are summarized in Table 1.

TABLE 1. *Electrode displacement values for different imaging resolutions*

FWHM, μm	Mean	90%	50%
0	0.60	0.0	0.0
80	1.07	0.0	0.0
160	10.72	32.4	1.0
240	22.3	56.8	14.8

All 3 error metrics go up as the resolution goes down. First column, FWHM of PSF for spatial blur, 2nd column, expected displacement magnitude, 3rd and 4th columns, 90th and 50th percentile displacement. FWHM, Full-width half-maximum; PSF, point spread function.

that the spatial distribution of MUA has little effect on the error, given the virtual absence of displacement under perfect imaging resolution (i.e., FWHM = 0 mm, shown by dark blue bars).

DISCUSSION

We present a novel method that allows the electrophysiological recording of neuronal responses from identified locations within V1 functional maps. The method circumvents the problems involved in the visual targeting of electrodes and is shown to be extremely robust to noise. Alternative methods have been described which localize multiple electrodes at desired locations in the maps, by way of electrode guide tubes (Niessing and Schmidt 2003; Schmidt et al. 2001). The method described here is more accurate, economical, and time-efficient than these prior techniques. The error analysis in Niessing et al. estimates that the electrodes deviate from the determined location by ~100 μm. Our first and second simulations estimate the deviation to be ~33 and ~22.3 μm, respectively. Niessing et al. also stated that the preparation requires ~16 h. Our electrode alignment does not require any experimental preparation in addition to the independent requirements of the electrophysiology and imaging. The algorithm is performed off-line and takes a matter of minutes. Although this technique does not allow for targeting of predetermined locations within the map, the electrodes invariably penetrate a variety of orientation map motifs for a given array insertion.

Although we used orientation maps to perform the alignment, it is clear that other feature maps could be used as well, including ocular dominance, retinotopy, and spatial frequency. Clearly, the more data one has, the better the alignment procedure is expected to perform. The method's use is not restricted to visual cortex and could find applicability in other cortical areas where topographic maps can be imaged. Finally, the method could be extended to situations where the array size is large enough so that the local shape of the cortex deviates significantly from planar. To do this, one could image the surface vasculature from a number of different viewpoints and use some salient key points, easily identifiable in all the images, to reconstruct the 3-D structure of the cortical surface (e.g., Hartley and Zisserman 2004; Tomasi and Kanade 1992). To show the feasibility of this approach, we selected 25 identifiable key points in six different frames obtained form different viewpoints (Fig. 8*A*). A natural selection of key points consists of the branching of blood vessels. Once the key points are identified in all the frames, we used the factorization

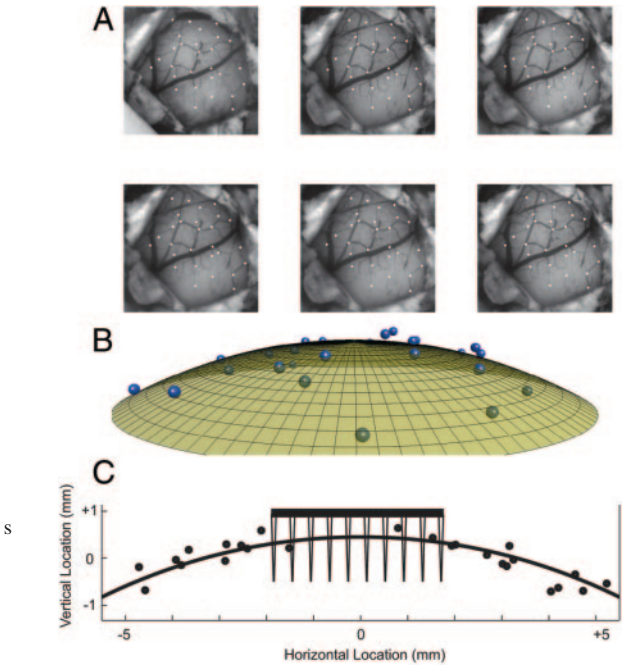

FIG. 8. Reconstruction of the cortical surface from multiple views. *A*: multiple key-points, normally associated with the bifurcation of blood vessels, are identified in frames corresponding to different views of the same cortical patch. Images appear similar to the eye because viewpoints differ from each other by ~10°. *B*: using the matrix factorization method of Tomasi and Kanade, one can reconstruct the 3-dimensional points in space. The surface represents the best approximation of a sphere to the data points. Radius of sphere is 12.4 mm. *C*: same data are shown in a projection over the azimuth dimension, along with the size of the array used in our experiments and typical insertion depth.

method of Tomasi and Kanade (1992) to reconstruct the 3-D location of points in space (Fig. 8*B*). The points, in this particular experiment, could be approximated as lying on top of a sphere of diameter 25 mm (Fig. 8*B*). Figure 8*C* shows the points and fitted sphere, projected over the azimuth dimension in spherical coordinates. For reference, the array used is shown to scale at a typical insertion depth. This shows that a geometric reconstruction of the cortical surface is possible through the identification of a number of key points from slightly different camera views. Once a geometric model of the cortical surface is at hand, a search for the location of the array could be performed taking the surface geometry into consideration.

We believe that the simplicity of the method and its straightforward implementation will provide a better experimental handle to study the relationship between cell receptive field properties and surrounding functional map organization. Studying such relationships may provide insight into how local cortical networks influence the tuning properties of cortical neurons.

ACKNOWLEDGMENTS

We thank B. Malone and A. Henrie for data collection and valuable comments and discussions. We also thank Y. Weiss and A. Gruber for sharing Matlab code implementing the Tomasi/Kanade factorization algorithm.

GRANTS

This work was supported by National Eye Institute Grant EY-12816 and Defense Advanced Research Projects Agency Grant FA8650-06-C-7633.

REFERENCES

Bonhoeffer T, Grinvald A. Iso-orientation domains in cat visual cortex are arranged in pinwheel-like patterns. *Nature* 353: 429–431, 1991.

Callaway E. Local circuits in primary visual cortex of the macaque monkey. *Annu Rev Neurosci* 21: 47–74, 1998.

Das A, Gilbert CD. Topography of contextual modulations mediated by short-range interactions in primary visual cortex. *Nature* 399: 655–661, 1999.

Dragoi V, Rivadulla C, Sur M. Foci of orientation plasticity in visual cortex. *Nature* 411: 80–86, 2001.

Ferster D, Miller K. Neural mechanisms of orientation selectivity in the visual cortex. *Annu Rev Neurosci* 23: 441–471, 2000.

Fitzpatrick D, Lund JS, Blasdel GG. Intrinsic connections of macaque striate cortex: afferent and efferent connections of lamina 4C. *J Neurosci* 5: 3329–3349, 1985.

Gray CM, Madonado PE, Wilson M, McNaughton B. Tetrodes markedly improve the reliability and yield of multiple single-unit isolation from multi-unit recordings in cat striate cortex. *J Neurosci Methods* 63: 43–54, 1995.

Grinvald A, Shoham D, Shmuel A, Glaser D, Vanzetta I, Shtoyermann E, Slovin H, Sterkin A, Wijnbergen C, Hildesheim R, Arieli A. *Modern Techniques in Neuroscience Research*, editor by Windhorst U and Johansson H. New York: Springer, 1999, p. 893–969.

Hartley RI, Zisserman A. *Multiple View Geometry.* Cambridge, UK: Cambridge, 2004.

Hetherington PA, Swindale NV. Receptive field and orientation scatter studied by tetrode recordings in cat area 17. *Vis Neurosci* 16: 637–652, 1999.

Hubel DH, Wiesel TN. Receptive fields, binocular interaction and functional architecture in the cat's visual cortex. *J Physiol* 160: 106–154, 1962.

Kelly RC, Smith MA, Samonds JM, Kohn A, Bonds AB, Movshon JA, Lee TS. Comparison of recordings from microelectrode arrays and single electrodes in the visual cortex. *J Neurosci* 27: 261–264, 2007.

Lund JS. Local circuit neurons of macaque monkey striate cortex: neurons of laminae 4C and 5A. *J Comp Neurol* 257: 60–92, 1987.

Maldonado PE, Godecke I, Gray CM, Bonhoeffer T. Orientation selectivity in pinwheel centers in cat striate cortex. *Science* 276: 1551–1555, 1997.

Mardia KV. *Statistics of Directional Data.* London: Academic, 1972.

Marino J, Schummers J, Lyon DC, Schwabe L, Beck O, Wiesing P, Obermayer K, Sur M. Invariant computations in local cortical networks with balanced excitation and inhibition. *Nat Neurosci* 8: 194–201, 2005.

McLaughlin D, Shapley R, Shelley M, Wielard DJ. A neuronal network model of macaque primary visual cortex (V1): orientation selectivity and dynamics in the input layer 4Cα. *Proc Natl Acad Sci USA* 97: 8087–8092, 2000.

McLaughlin D, Shapley R, Shelley M. Large-scale modeling of the primary visual cortex: influence of cortical architecture upon neuronal response. *J Physiol Paris* 237–252, 2003.

Niessing M, Schmidt K, Singer W, Galuske R. Precise placement of multiple electrodes into functionally predefined cortical locations. *J Neurosci Methods* 126: 195–207, 2003.

Ohki K, Chung S, Ch'ng YH, Kara P, Reid CR. Functional imaging with cellular resolution reveals precise micro-architecture in visual cortex. *Nature* 433: 597–603, 2005.

Ohki K, Chung S, Kara P, Hubener M, Bonhoeffer T, Reid CR. Highly ordered arrangement of single neurons in orientation pinwheels. *Nature* 442: 925–928, 2006.

Orbach H, Cohen L. Optical monitoring of activity from many areas of the in vitro and in vivo salamander olfactory bulb: a new method for studying functional organization in the vertebrate central nervous system. *J Neurosci* 13: 2251–2262, 1983.

Polimeni JR, Granquist-Fraser D, Wood RJ, Schwartz EL. Physical limits to spatial resolution of optical recording: clarifying the spatial structure of cortical hypercolumns. *Proc Natl Acad Sci USA* 102: 4158–4163, 2005.

Rall W. Electrophysiology of a dendritic neuron model. *Biophys J* 2: 145–167, 1962.

Ringach D, Hawken M, Shapley R. Dynamics of orientation tuning in macaque V1: the role of global and tuned suppression. *J Neurophysiol* 90: 342–352, 2003.

Ringach D, Sapiro G, Shapley R. A subspace reverse-correlation technique for the study of visual neurons. *Vision Res* 17: 2455–2464, 1997.

Rousche PJ, Normann RA. A method for pneumatically inserting an array of penetrating electrodes into cortical tissue. *Ann Biomed Eng* 20: 413–422, 1992.

Schummers J, Marino J, Sur M. Synaptic integration by V1 neurons depends on location within the orientation map. *Neuron* 36: 969–978, 2002.

Schmidt KE, Grün S, Singer W, Galuske RAW. Parallel multi-unit recordings in primary visual cortex of the unrestrained awake and sleeping cat. *Soc Neurosci Abstr* 27: 821.58, 2001.

Shapley R, Hawken MJ, Ringach DL. Dynamics or orientation tuning in the primary visual cortex and the importance of cortical inhibition. *Neuron* 38: 689–699, 2003.

Sompolinsky H, Shapley RM. New perspectives on the mechanisms for orientation selectivity. *Curr Opin Neurobiol* 7: 514–522, 1997.

Tomasi C, Kanade T. Shape and motion from image streams under orthography: a factorization approach. *Int J Comp Vision* 9: 137–154, 1992.

Yoshioka T, Blasdel GG, Levitt JB, Lund JS. Relation between patterns of intrinsic lateral connectivity, ocular dominance, and cytochrome oxidase-reactive regions in macaque monkey striate cortex. *Cereb Cortex* 2: 297–310, 1996.